J Supercond Nov Magn (2012) 25:1913–1920
DOI 10.1007/s10948-012-1511-7

ORIGINAL PAPER

Structural, Magnetic and Electrical Properties of Cu Substituted Mn–Zn Soft Nanoferrites

Humaira Anwar · Asghari Maqsood

Published online: 18 March 2012

Abstract Soft nanoferrites of nominal composition $Mn_{0.5}Cu_xZn_{0.5-x}Fe_2O_4$ with $0.0 \leq x \leq 0.35$ were prepared by chemical co-precipitation method. The formation of single phase spinel structure with different compositions, sizes and macrostructure were confirmed by X-ray diffraction patterns and scanning electron microscopic (SEM) measurements. The lattice parameter decreased with increase in Cu^{2+} content. The crystallite size of the powder samples varied from 14 to 27 nm. The theoretical density increased with increase in Cu^{2+} content. Room temperature saturation magnetization was measured as a function of copper content. The saturation magnetization (*Ms*) and Bohr magneton (μ_B) increases up to $x = 0.25$ due to increased A–B interactions in the AB_2O_4 type spinel nanoferrites. Dielectric permittivity, dielectric loss tangent and complex impedance plots were studied in the frequency range 20 Hz–5 MHz. Loss peak occurs for all the studied compositions and shifts towards low frequency with increased Cu^{2+} content. Complex impedance spectroscopic studies confirmed that conduction in the samples is due to grain boundaries. The high values of DC electrical resistivity support this result.

Keywords Nanoferrite · X-ray diffraction · Magnetization · Dielectric constant · Dielectric loss tangent · Complex impedance

H. Anwar · A. Maqsood (✉)
Thermal Transport Laboratory, School of Chemical and Materials Engineering (SCME), National University of Sciences and Technology, H-12, Islamabad, Pakistan
e-mail: tpl.qau@usa.net

H. Anwar
e-mail: merey_anwar@yahoo.com

1 Introduction

Magnetic and semiconducting ferrospinels have a wide range of potential applications, due to their interesting physical, structural, magnetic and electrical properties. Magnetic ferrites possess high DC electric resistivity, low eddy current and low dielectric losses [1, 2]. They are extensively used in microwave devices, information storage systems, magnetic cores, several medical diagnostic purposes, etc. [3]. Mn–Zn ferrites can be divided into two groups [4], high permeability materials that are used at low frequencies. The grain boundaries represent obstacles to domain movement, thus decreasing the permeability. The ferrites should therefore be coarse grained to display a high permeability. Power ferrites are used at high frequencies (∼1 MHz) and exhibit low power losses. In contrast to high-permeability ferrites, the grain boundaries in power ferrites should exhibit a high resistivity in order to decrease power losses [5]. Different techniques such as hydrothermal, sol–gel, co-precipitation, combustion reaction, mechano-chemical and micro-emulsion [6–9] methods have been developed to synthesize nanoparticles of spinel ferrite. In the spinel type structure, cations and anions are distributed between two different lattice sites: tetrahedral (A) and octahedral (B) sites. Electrical properties as well as magnetic properties of these ferrites strongly depend on the distribution of cations at different sites as well as the preparation methods, sintering temperature, substitution elements and different conditions [5]. Many researchers have studied structural, magnetic and electrical properties of Mn–Zn and Mn–Zn substituted ferrites [10–13].

Manganese ferrite is inverse spinel and zinc ferrite is normal spinel. Substitution of small amount of cations improve the electrical and magnetic properties of these ferrites. We have synthesized complex spinel nanoferrites of $Mn_{0.5}Cu_xZn_{0.5-x}Fe_2O_4$ with variation of concentration x

by chemical co-precipitation method. The prepared nanoferrites are characterized by X-rays diffraction (XRD), infrared spectroscopy (IR), scanning electron microscopy (SEM), vibrating sample magnetometer (VSM), impedance studies by LCR meter and two probe resistivity apparatus to investigate the compositional, structural, morphological, magnetic and electrical properties.

2 Experimental Details

2.1 Synthesis

Crystalline ferrospinels were synthesized by the chemical co-precipitation method. High purity (AR grade) ferric nitrate, copper nitrate, zinc nitrate, manganese nitrate and sodium hydro-oxide were used as raw materials. Stoichiometric amounts of individual metal nitrates were dissolved in minimum quantity [0.05 molar solutions of $Mn(NO_3)_2 \cdot 4H_2O$, 0.05 molar $Zn(NO_3)_2 \cdot H_2O$ and 0.2 molar $Fe(NO_3)_2 \cdot 9H_2O$] of doubly distilled de-ionized water to get a clear, transparent solution at 85 °C. To this, 3 molar sodium hydro-oxide solution was added drop wise with constant stirring. The pH of the solution was maintained between 10.5–11.5. The mixture was then heated at 90 °C for about 1 h. The precipitates were thoroughly washed with distilled water, at least five washings, until the washings were free from sodium and chloride ions. The product was dried in an electric oven at 105 °C for overnight to remove water contents. All the synthesized samples were sintered at 450 °C for 4 h. The sintered ferrites were mixed with 2 % PVA as binder and pressed into pellets of 13 mm diameter by applying a uniaxial load of 5 kN using hydraulic press. These pellets were gradually heated to about 300 °C to remove the binder. The powder form of the samples was used for structural and magnetic study, while pellets were utilized for dielectric measurements.

2.2 Characterizations

X-ray powder diffraction study was performed with CuKα radiation ($\lambda = 1.54056$ Å) to identify the phases and to calculate the lattice constant. Particle size analysis was carried out using a scanning electron microscope (JEOL-instrument JSM-6490A), with an accelerating voltage of 30 kV. Lattice constant was determined using the relation $\frac{1}{d^2} = \frac{h^2+k^2+l^2}{a^2}$ where a is the lattice constant, $(h\ k\ l)$ are the Miller indices and d is the inter planar distance. Crystallite size was calculated using Scherrer's relation [14]:

$$t = \frac{0.98\lambda}{\beta \cos\theta} \tag{1}$$

where t is the crystallite size, λ the X-ray wavelength of CuKα radiation and β is the full width at half maximum (FWHM) in radians of the XRD peak at 2θ. The X-ray density of the prepared samples was calculated using the relation [15]:

$$D_x = \frac{8M}{Na^3} \tag{2}$$

where M is the molecular weight and N is the Avogadro's number. The measured density is calculated assuming the cylindrical shape of the pellets and using the relation [15]:

$$D_m = \frac{m}{V} = \frac{m}{\pi r^2 l} \tag{3}$$

here m, r and l are the mass, radius and thickness of the pellet respectively. The percentage porosity was calculated using the relation [15]:

$$P = \left(1 - \frac{D_m}{D_x}\right) \times 100 \tag{4}$$

Infrared absorption spectra (FTIR) of samples with varying copper concentration were recorded in the range of 400–700 cm^{-1} at room temperature. Magnetic measurements give information about the magnetic ordering present in a magnetic material. Magnetic measurements for all the compositions were performed at room temperature using a vibrating sample magnetometer (VSM), BHV 50, Riken Denshi Co. Ltd. Japan. Different magnetic parameters e.g. saturation magnetization (Ms), remanence (Mr), coercivity (Hc) etc. were calculated using M–H loop. The DC electrical resistivity was measured by a simple two-probe method within temperature range 300–573 K. The relation between resistivity and temperature [16] may be expressed as

$$\rho = \rho_o e^{\frac{\Delta E}{k_B T}} \tag{5}$$

Dielectric constant (ε') in ferrites is contributed by several structural and micro-structural factors. Frequency dependent dielectric constant, dielectric loss tangent and complex impedance were measured in the frequency range 20 Hz–5 MHz by (Wayne Kerr 6500B) LCR precision meter bridge in the parallel mode. Silver paste was applied on both sides of the pellet for good ohmic contacts. Dielectric constant (ε') and loss tangent ($\tan\delta$) of the samples is calculated using the relations [14, 17]:

$$\varepsilon' = \frac{Cd}{\varepsilon_o A}, \tag{6}$$

$$\tan\delta = \frac{1}{2\pi f \varepsilon_o \epsilon' \rho} \tag{7}$$

where C is the capacitance of the pellet, d the thickness, A the cross sectional area of the flat surface pellet, ε_o the dielectric permittivity of the free space, ρ is the resistivity and f the frequency of applied field. The complex impedance spectroscopy is a powerful tool to study the relaxation phenomenon. The impedance measurements were carried out at room temperature in the frequency range from 20 Hz to 5 MHz.

3 Results and Discussion

3.1 Structural analysis

The X-ray diffraction pattern of ferrite samples having general formula $Mn_{0.5}Cu_xZn_{0.5-x}Fe_2O_4$ where $x = 0.0$, 0.15, 0.25 and 0.35 are shown in Fig. 1. The peaks could be indexed as (2 2 0), (3 1 1), (4 0 0), (4 2 2), (5 1 1), (4 4 0) and (5 3 3), which are characteristics of single-phase spinel structure. The variation of lattice constant with Cu concentration is listed in Table 1. The lattice constant decreased with increase in Cu^{2+}, which is due to replacement of larger cations Zn^{2+}(0.82 Å) by smaller cations Cu^{2+}(0.72 Å) [16]. The average crystalline sizes were determined using Scherrer's formula [15]. The crystallite size remained within the range 14 to 27 nm for the studied samples. The lattice constant a, measured density Dm, X-ray density Dx and porosity P are listed in Table 1. The Dx increased from 5.235 to 5.299 g-cm^{-3}, with concentration x in the prepared nanoferrites. Since Cu has relatively smaller atomic mass (63.546 amu) than Zn (65.390 amu) atoms, which subsequently influenced the density due to the increase in mass which overtook the decrease in volume of the unit cell.

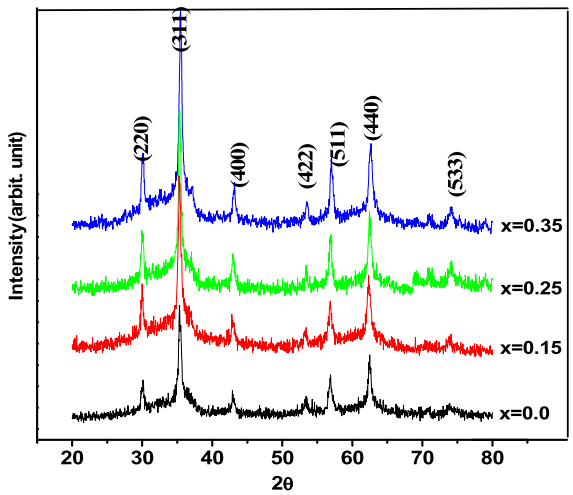

Fig. 1 X-ray diffraction patterns of $Mn_{0.5}Cu_xZn_{0.5-x}Fe_2O_4$ ferrite samples

3.2 Scanning Electron Micrograph Study

Figure 2 shows the scanning electron micrograph (SEM) of $Mn_{0.5}Cu_xZn_{0.5-x}Fe_2O_4$ system ($x = 0.15$). It is evident that the synthesized sample has spherical particles shape ranging in sizes from 12 to 35 nm. Most of the particles are about 22 nm in size. This is in good agreement with the average crystallite size (21 nm) obtained from X-ray measurements shown in Table 1.

3.3 FTIR Studies

Figure 3 shows the IR spectrum for the samples with different copper content. It is known that the high wave number band ν_1 in ferrites appeared at 500–600 cm^{-1} represent the tetrahedral complexes, while the lower wave number ν_2 at 400–450 cm^{-1} represent the octahedral complexes [18, 19]. Therefore in the investigated samples, the high wave number ν_1 represents the vibration of Fe^{3+}–O^{2-} in the sub-lattice site A, while the lower wave number band ν_2 represents the trivalent metal–oxygen vibrations at the octahedral B-sites. The FTIR transmission spectrum revealed two dominant absorption bands ranging from 602–581 cm^{-1} (ν_1) and

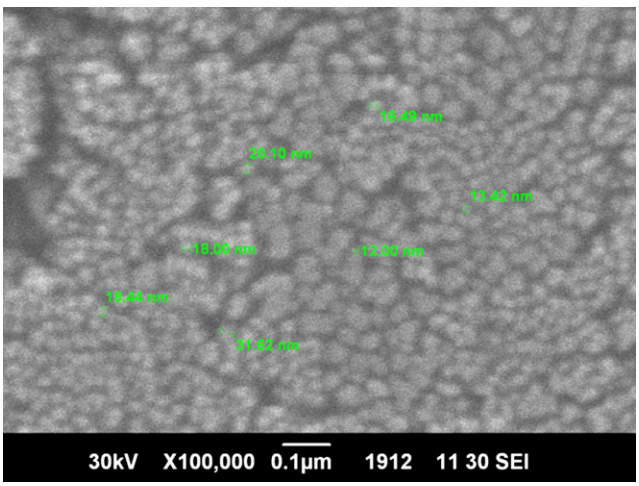

Fig. 2 SEM image of $Mn_{0.5}Cu_xZn_{0.5-x}Fe_2O_4$ ferrite sample ($x = 0.15$)

Table 1 The average crystallite size (t (ave)), lattice constant (a), X-rays density (D_x), measured density (D_m), porosity (P), DC electrical resistivity (ρ_{DC}), activation energy (ΔE) of the $Mn_{0.5}Cu_xZn_{0.5-x}Fe_2O_4$ nanoferrites with varying concentrations $0 \le x \le 0.35$

Composition	$x = 0.0$	$x = 0.15$	$x = 0.25$	$x = 0.35$
t (311) (nm)	14	22	27	25
a (Å)	8.431	8.408	8.405	8.389
D_x (g-cm^{-3})	5.235	5.272	5.274	5.299
D_m (g-cm^{-3})	3.732	3.621	3.590	3.641
Porosity (%)	28.7	31.3	31.9	31.3
ρ (Ω-cm) at 373 K	5.32×10^8	7.14×10^9	6.67×10^9	4.52×10^9
ΔE (eV)	0.70	0.62	0.63	0.53

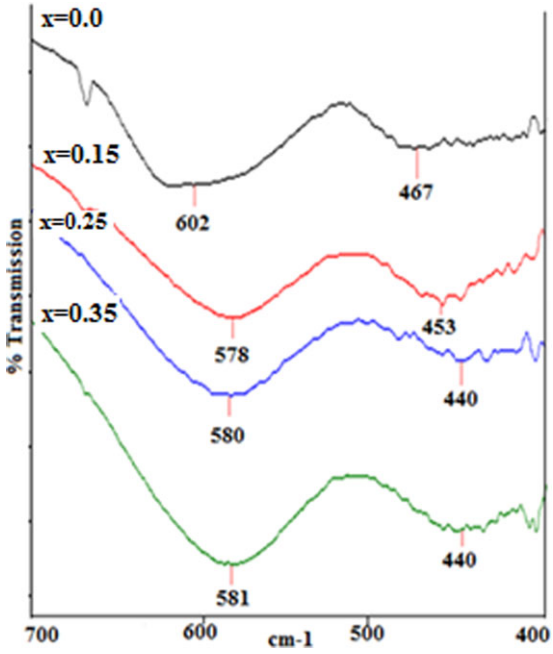

Fig. 3 FT-IR for $Mn_{0.5}Cu_xZn_{0.5-x}Fe_2O_4$ ferrite samples

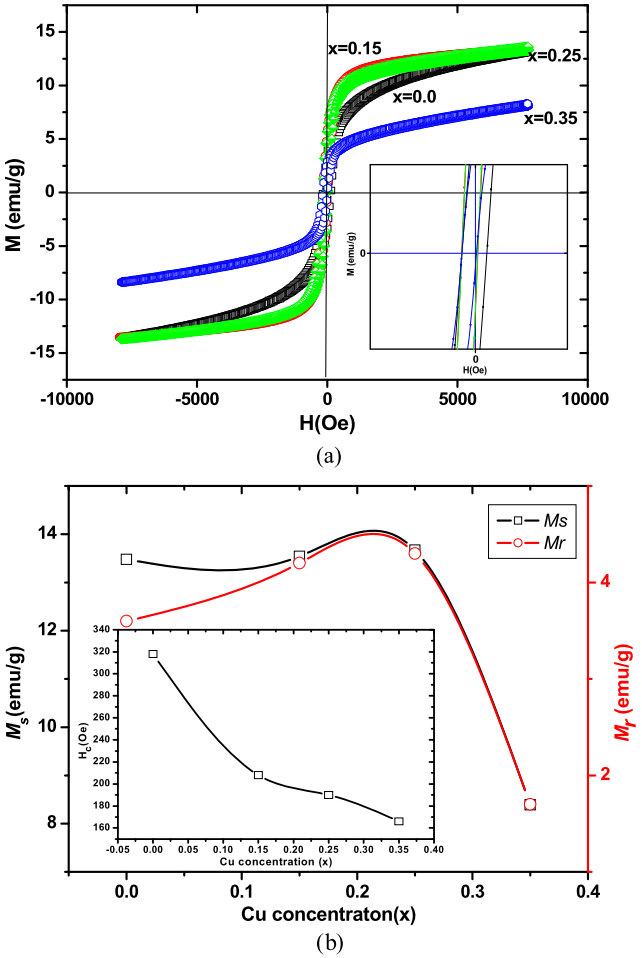

Fig. 4 (**a**) Hysteresis curves for $Mn_{0.5}Cu_xZn_{0.5-x}Fe_2O_4$ ferrite samples, (**b**) Change in saturation magnetization (*Ms*) and remanent magnetization (*Mr*) with Cu^{2+} concentration. *Inset* shows variation of coercivity with Cu^{2+} concentration

467–440 cm^{-1} (ν_2) due to tetrahedral Fe^{3+}–O^{2-} and octahedral sites for $Mn_{0.5}Cu_xZn_{0.5-x}Fe_2O_4$ ferrite powder, respectively. Shifting of tetrahedral and octahedral bands towards lower wavelength side with increase in Cu^{2+} content is observed. The difference in ν_1 and ν_2 band positions is expected because of the difference in the Fe^{3+}–O^{2-} distances for the octahedral and the tetrahedral sites due to redistribution of cations with the substitution of Cu^{2+} ions.

3.4 Magnetic Studies

The M–H loops for all the samples have been plotted as shown in Fig. 4(a). The low value of coercivity indicates the soft nature of ferrites. It is observed that the saturation magnetization increases slowly with increase in Cu^{2+} concentration up to $x = 0.25$ in the composition $Mn_{0.5}Cu_xZn_{0.5-x}Fe_2O_4$ and starts decreasing after wards. The decrease in magnetization is observed for $x > 0.25$ could be attributed to decrease in A–B type interaction in Cu^{2+} substituted Mn–Zn structure. It is observed that saturation magnetization of Cu^{2+} (13.67 emu/g) added ferrite is higher than pure Mn–Zn (13.48 emu/g). Similar increase in saturation magnetization with Ni–Cu–Zn has been reported by Rahman and Roy et al. [20, 21].

The variation in saturation magnetization with Cu^{2+} content is shown in Fig. 4(b). This could be explained by cation distribution and exchange interaction, since the cations distribution at A- and B-sites greatly influence the magnetic properties of ferrites. It is well known that Zn^{2+} ion has strong A-site occupancy, Mn^{3+} ions prefer to go at B-sites, while Cu^{2+} and Fe^{3+} ions can occupy both A and B-sites [22]. Substitution of Cu^{2+} in place of Zn^{2+} results into migration of some of Fe^{3+} ions from B to A-site. This process will increase the magnetization of Mn–Zn ferrites. At high concentration of Cu^{2+} ions ($x > 0.25$), formation of Fe^{2+} ions and B–B super-exchange interaction reduces the overall magnetization of ferrites. Both these factors lower the saturation magnetization of Cu doped Mn–Zn ferrites [23–25].

The magnetic moment (μ_B) was calculated from the relation

$$\mu_B = \frac{M.W \times Ms}{5585 \times \rho_m} \tag{8}$$

where $M.W$, Ms, and ρ_m are the molecular weight, saturation magnetization, and measured density. The Bohr magneton values are illustrated in Table 2. The results obtained are in agreement with previous studies of ferrites containing Mn, Cu, or Zn ions [26–30]. In calculating the magnetic moment (μ_B), we have considered A–B interaction and cations distribution. It is observed that due to the substitu-

Table 2 Coercivity (H_c), saturation magnetization (M_s), remnant magnetization (M_r), Bohr's magneton (μ_B), Y-K angle ($\alpha_{Y\text{-}K}$) (degree), squareness ratio (Mr/Ms) of the $Mn_{0.5}Cu_xZn_{0.5-x}Fe_2O_4$ nanoferrites with varying concentrations $0 \le x \le 0.35$

Composition	$x = 0.0$	$x = 0.15$	$x = 0.25$	$x = 0.35$
H_c (Oe)	318	208	190	166
M_s (emu/g)	13.48	13.54	13.67	8.39
M_r (emu/g)	3.6	4.2	4.3	1.7
μ_B	0.21	0.22	0.23	0.13
$\alpha_{Y\text{-}K}$	30	43	50	58
M_r/M_s	0.26	0.31	0.31	0.20

tion of Cu^{2+} ions at tetrahedral (A) and octahedral (B) sites in place of Zn^{+2} ions, the magnetic moment of octahedral B-site increases. This is in agreement with the observations in [30]. The decrease in n_B for $x > 0.25$ Cu^{2+} content is due to weakening of A–B interactions and change of B–B interactions from ferromagnetic to antiferromagnetic state [27].

The Yafet–Kittel (Y-K) angles have been calculated using the formula [31]

$$\mu_B = (6 + x)\cos\alpha_{Y-K} - 5(1 - x) \tag{9}$$

where x represents the Cu^{2+} concentration. The vales of Y-K angles are illustrated in Table 2. The increase in Y-K angle with increase in Cu^{2+} content suggests the canted spin model of magnetization in these ferrites and increased B–B super exchange interactions [32]. The increase in Y-K angle with Cu^{2+} concentration indicates the fact that triangular spin arrangement is suitable on the B-site leading to reduction in A–B interaction. It is also clear in the present system of ferrites that randomness increases as Cu^{2+} is substituted in these ferrites and shows a significant departure from the Néel collinear model.

3.5 Dielectric Study

The frequency dependence of the dielectric constant for samples have been studied in the frequency range from 20 Hz to 5 MHz. Figure 5(a) shows the variation of dielectric constant with frequency for different concentrations of Cu^{2+}. It is clear that the samples exhibit the dielectric dispersion where dielectric constant (ε') decreases as the frequency increases from 20 Hz–5 MHz. The dielectric constant decreases rapidly in low frequency region and slows down in high frequency region, almost approaches frequency independent behavior. The phenomenon of dielectric dispersion in ferrites has been explained on the basis of Maxwell–Wagner model [33, 34] and Koop's phenomenological theory [35] of dielectrics. This model suggests that dielectric medium is made of well conducting grains, separated by poorly conducting grain boundaries. It has been observed that in ferrites the permittivity is directly

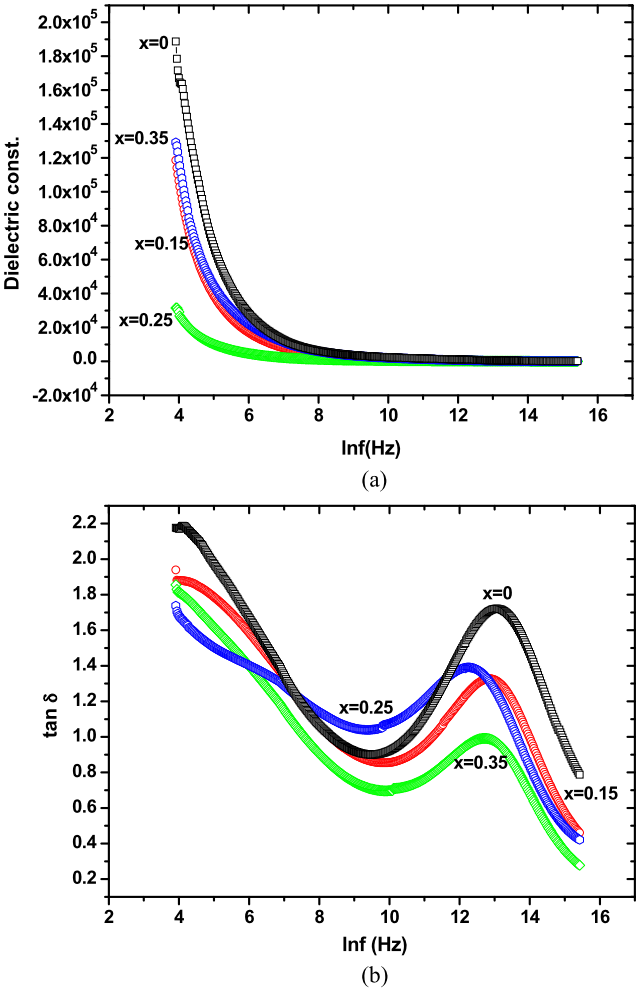

Fig. 5 Variation in (**a**) dielectric constant (ε') and (**b**) loss tangent ($\tan\delta$) for $Mn_{0.5}Cu_xZn_{0.5-x}Fe_2O_4$ ferrite samples

proportional to the square root of conductivity [36]. Therefore the grains are highly conductive and have high values of permittivity, while as the grain boundaries are less conductive and have smaller values of permittivity. At lower frequencies the grain boundaries are more effective than grains in electrical conduction. The thinner the grain boundary, the higher is the value of dielectric constant. The higher values of the dielectric constant (ε') observed at lower frequencies are also explained on the basis of interfacial/space polarization due to inhomogeneous dielectric structure [37, 38]. The inhomogeneities present in the system can be porosity and grain structure. The variation of dielectric loss tangent ($\tan\delta$) is shown in Fig. 5(b). It is observed that the loss tangent decreases initially with increasing frequency followed by the appearance of the relaxation peak. The appearance of relaxation peak can be explained according to the Debye relaxation theory [38]. The loss peak occurs when the applied field is in phase with the dielectrics and the condition $\omega\tau = 1$ is satisfied, where $\omega = 2\pi f$, f being the frequency of the applied field. Singh et al. [39] have observed a similar

relaxation peak at a frequency of 1 kHz for Mn substituted Ni–Zn ferrites synthesized by the citrate precursor method. In the present investigation, the relaxation peak appears at frequency 450 kHz and shifts towards lower frequency with increase in Cu^{2+} content. The shifting of the relaxation peak towards lower frequency side with an increase in Cu^{2+} is due to the strengthening of the dipole–dipole interactions causing hindrance to the rotation of the dipoles [39]. Therefore, the resonance between rotation of the dipoles and applied field takes place at lower frequency. Values of dielectric constant (ε') and loss tangent ($\tan\delta$) at 100 and 1 MHz are listed in Table 3. The results show decreased in dielectric constant and loss tangent with increase in Cu^{2+} content.

3.5.1 Impedance Spectroscopy

Figure 6 show the resistive (real Z') and imaginary (reactive Z'') part of impedance as a function of applied field for given compositions. The value of Z' and Z'' decreased with increase in frequency which shows ac conductivity increase with increasing frequency. The values of real and imaginary parts of impedance decreases except for $x = 0.25$. The increase in values of both parts of impedance for $x = 0.25$ is consistent with the results of dielectric measurements. The complex impedance measurements gives the information about real (resistive) and imaginary (reactive) components of a system. Impedance plane plots usually show two semicircular arcs, smaller one at high frequency and larger one at low frequency side. The semicircle at low frequency represent resistance of grain boundaries (R_{gb}) and one at high frequency gives resistance of grains (R_g) [40]. To correlate the electrical properties of the $Mn_{0.5}Cu_xZn_{0.5-x}Fe_2O_4$ composition with microstructure of the material, an equivalent circuit model shown in the inset of Fig. 7(a). In nanoferrites, the grain boundary resistance is higher than the grain resistance [41]. The parameters R_g, R_{gb}, C_g and C_{gb} were obtained by fitting the impedance plane plots using Zview software (within 2 % fitting error) for all the compositions and listed in Table 3. Figure 7(b) shows increase in resistance of both grains and grain boundaries up to $x \leq 0.25$ while decreases suddenly for $x > 0.25$. This increase in resistance with Cu^{2+} concentration is in good agreement with electrical measurements. In the present study appearance of one semicircle for all samples suggests a predominant contribution from the grain boundaries (Fig. 8). The calculated values support this statement.

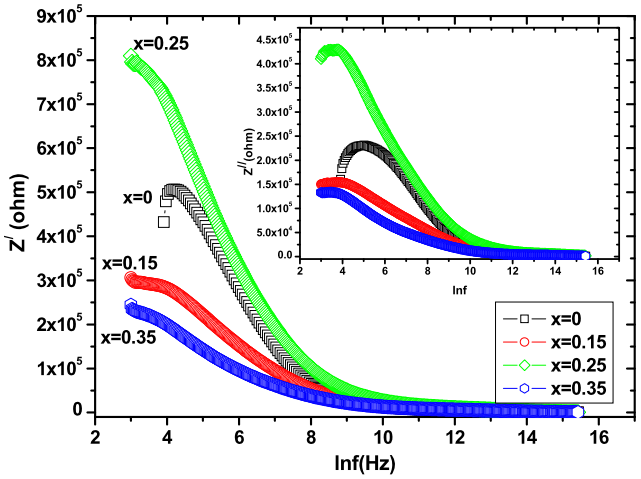

Fig. 6 Variation in resistive (Z') and reactive (Z'') (*inset*), parts of impedance of $Mn_{0.5}Cu_xZn_{0.5-x}Fe_2O_4$ ferrite samples

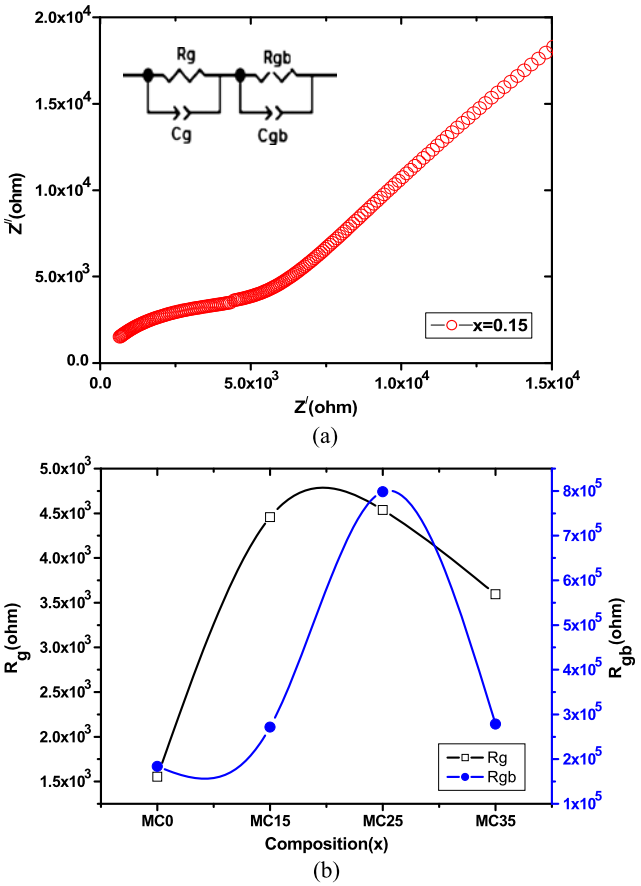

Fig. 7 (**a**) Complex impedance plane plot of $Mn_{0.5}Cu_{0.15}Zn_{0.35}Fe_2O_4$ ferrite samples. (**b**) Variation of grains and grain boundaries resistance with Cu concentration

3.6 Electrical Measurements

In general, DC electrical resistivity of ferrites depends on the crystalline size, chemical composition, density, porosity and sintering temperature. The DC electrical resistivity measurements were done using two probe method for all compositions and their values are given in Table 1. It is seen that DC electrical resistivity shows a linear decreasing behavior with increase in temperature Fig. 9, which confirms the semiconducting behavior for all the samples. The resis-

Table 3 Dielectric constant (ε'), loss tangent ($\tan\delta$), resistive impedance (Z'), reactive impedance (Z''), resistance of grains (R_g) and grain boundaries (R_{gb}) of the $Mn_{0.5}Cu_xZn_{0.5-x}Fe_2O_4$ nanoferrites with varying concentrations $0 \leq x \leq 0.35$

Composition	$x = 0.0$	$x = 0.15$	$x = 0.25$	$x = 0.35$
ε' at (100 Hz)	1.01×10^5	5.55×10^4	1.45×10^4	6.25×10^4
ε' at (1 MHz)	3.06×10^2	1.86×10^2	8.1×10^1	1.87×10^2
$\tan\delta$ at (100 Hz)	2.09	1.84	1.70	1.56
$\tan\delta$ at (1 MHz)	1.54	1.07	0.75	0.91
Z' at (100 Hz)	4.81×10^5	2.49×10^5	5.89×10^5	1.64×10^5
Z'' at (100 Hz)	2.27×10^5	1.44×10^5	3.81×10^5	1.11×10^5
Z' at (1 MHz)	1.65×10^3	3.10×10^3	3.47×10^3	2.48×10^3
Z'' at (1 MHz)	1.64×10^3	3.13×10^3	5.01×10^3	3.00×10^3
R_g (ohm)	1.55×10^3	4.46×10^3	4.54×10^3	3.59×10^3
R_{gb} (ohm)	1.80×10^5	2.70×10^5	7.98×10^5	2.80×10^5
C_g (Farad)	7.98×10^{-10}	1.32×10^{-10}	1.29×10^{-11}	5.86×10^{-11}
C_{gb} (Farad)	3.30×10^{-9}	1.16×10^{-8}	6.68×10^{-9}	5.44×10^{-8}

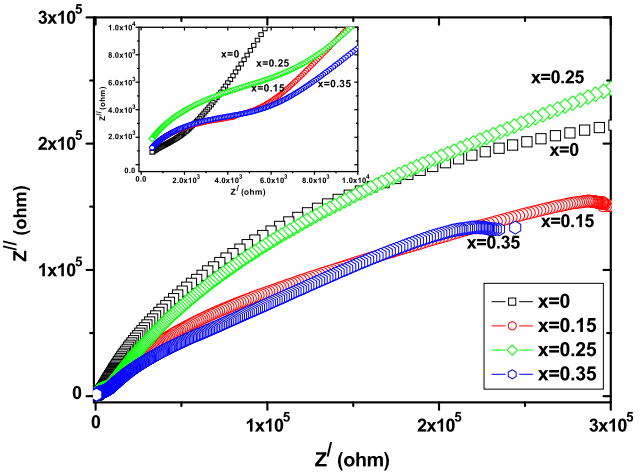

Fig. 8 Complex impedance plane plots of $Mn_{0.5}Cu_xZn_{0.5-x}Fe_2O_4$ ferrite samples. Inset shows the equivalent circuit model

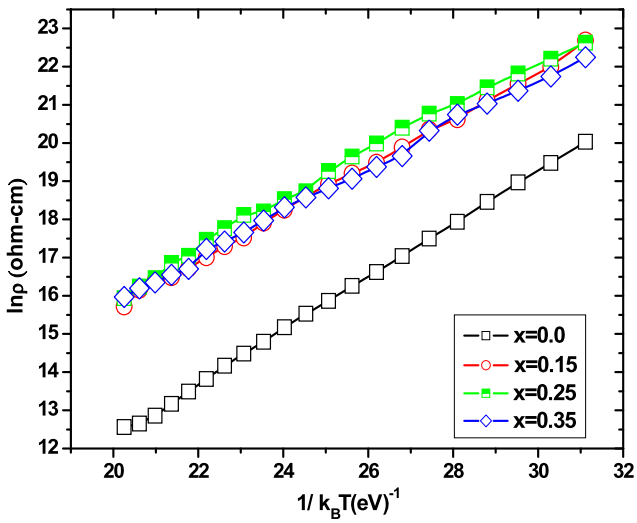

Fig. 9 DC electrical resistivity of $Mn_{0.5}Cu_xZn_{0.5-x}Fe_2O_4$ ferrite samples

tivity increases with Cu^{2+} concentration up to $x < 0.25$ to the value of 7.14×10^9 Ω-cm at 373 K. This high value of DC electrical resistivity is attributed due to large number of grain boundaries at nanoscale. The increase in electrical resistivity with Cu^{2+} content is mainly due to redistribution of iron ions at A and B sites. Cu^{2+} ions prefer to occupy B-sites replacing Fe^{3+} ions which have equal tendency to occupy both A and B sites. Moreover, the existence of Mn^{2+} and Mn^{3+} ion pairs gives rise to the A–B hopping mechanism. The activation energy ΔE was calculated using slope of the curve between $\ln\rho$ vs. $1/k_BT$ plot. ΔE decreases with increase in Cu^{2+} concentration showing that conduction is due to hopping of electrons.

4 Conclusions

Copper substituted Mn–Zn soft ferrites with composition $Mn_{0.5}Cu_xZn_{0.5-x}Fe_2O_4$ with a concentration $0.00 \leq x \leq 0.35$ were prepared via a chemical co-precipitation method. Single phase spinel structure of the compound was confirmed by X-ray diffraction with the size of the nanoferrites in the range of 14–27 nm which is in agreement with SEM results. The lattice constant was found to decrease with increase in the Cu^{2+} content. This observation is attributed due to the relative smaller ionic radii of Cu^{2+} as compared to Zn^{2+}. The observed results suggest that the morphology and structure of the synthesized nanoferrites can be controlled by varying the composition in $Mn_{0.5}Cu_xZn_{0.5-x}Fe_2O_4$. Higher and lower frequency bands attributed to positions of cations, e.g., tetrahedral and octahedral sites of the prepared spinel-ferrites were observed using FTIR spectroscopy. A slight variation in the bands is attributed to the relative size variation between Cu^{2+} and Zn^{2+} metal ions. Furthermore, the hysteresis loop indicates the soft nature of prepared nanoferrites. Saturation magneti-

zation (*Ms*), remanence (*Mr*), coercivity (*Hc*) and magnetic moment (μ_B) are calculated from the hysteresis loop and found to increase with Cu^{2+} concentration up to $x = 0.25$ in the prepared nanoferrites. The Y-K angle strongly varies with composition showing spin canting nature of magnetization. Dielectric and complex impedance plane plots show the major contribution due to grain boundaries resistance. The results are in agreement with DC electrical measurements.

Acknowledgements Authors are thankful to Higher Education Commission (HEC) Pakistan for supporting this research work through 5000 Indigenous Scholarships (Batch-V) and Pakistan Science Foundation (PSF) project No. 147.

References

1. Watawe, S.C., Bamane, U.A., Gonbare, S.P., Tangoli, R.B.: Mater. Chem. Phys. **103**, 323 (2007)
2. Kharabe, R.G., Devan, R.S., Kanamadi, C.M., Chougule, B.K.: Smart Mater. Struct. **15**, 125 (2006)
3. Igarashi, H., Okazaki, K.: J. Am. Ceram. Soc. **60**, 51–54 (1977)
4. Vladikova, D., Ilkov, L.: Phys. Solid State **111**, 145–154 (1989)
5. Hudson, A.S.: Marconi Rev. **37**, 43 (1968)
6. Dong, L.M., Han, Z.D., Zhang, Y.M.: J. Rare Earths **S1**, 54–56 (2006)
7. Li, S.M., Wang, Q., Wu, A.B.: Curr. Appl. Phys. **9**, 1386–1392 (2009)
8. Costa, A.C.F.M., Leite, A.M.D., Ferreira, H.S.: J. Eur. Ceram. Soc. **28**, 2033–2037 (2008)
9. Zhang, J.L., Shi, J.X., Gong, M.L.: J. Solid State Chem. **182**, 2135–2140 (2009)
10. Yan, M.F., Johnson, D.W.: J. Am. Ceram. Soc. **61**, 342–349 (1978)
11. Ammad, H., Qureshi: J. Cryst. Growth **286**, 365–370 (2006)
12. Zhu, J., Tseng, K.J.: IEEE Trans. Magn. **40**, 3339–3345 (2004)
13. Nie, J., Li, H., Feng, Z., He, H.: J. Magn. Magn. Mater. **265**, 172–175 (2003)
14. George, M., Nair, S.S., John, A.M., Joy, P.A., Anantharaman, M.R.: J. Phys. D, Appl. Phys. **39**, 900 (2006)
15. Gul, I.H., Abbasi, A.Z., Amin, F., Rehman, M.A., Maqsood, A.: J. Magn. Magn. Mater. **311**, 494 (2007)
16. Smit, J., Wijin, H.P.J.: Ferrites. Wiley, New York (1959)
17. Berchmans, L.J., Selvan, R.K., Kumar, P.N.S.: J. Magn. Magn. Mater. **279**, 103 (2004)
18. Shanon, R.D., Prewitt, C.T.: Acta Crystallogr. **1326**, 1026 (1970)
19. Rath, C., Anand, S., Das, R.P., Sahu, K.K., Kulkarni, S.D., Date, S.K., Mishra, N.C.: J. Appl. Phys. **91**, 2211–2215 (2002)
20. Rahman, I.Z., Ahmed, T.T.: J. Magn. Magn. Mater. **290–291**, 1576–1579 (2005)
21. Roy, P.K., Bera, J.: Mater. Res. Bull. **42**, 77–83 (2007)
22. Jing, J., Liangchao, L., Feng, X.: J. Rare Earths **25**, 79 (2007)
23. Verma, S., Karande, J., Patidar, A., Joy, P.A.: Mater. Lett. **59**, 2630 (2005)
24. Baruwati, B., Rana, R.K., Manorama, S.V.: J. Appl. Phys. **101**, 014302 (2007)
25. Joshi, G.K., Khot, A.Y., Sawant, S.R.: Solid State Commun. **65**(12), 1593–1595 (1988)
26. Duquea, J.G.S., Souzaa, E.A., Menesesa, C.T., Kubota, L.: J. Phys. B, At. Mol. Phys. **398**, 287–290 (2007)
27. Mansour, S.F.: J. Magn. Magn. Mater. **323**, 1735–1740 (2011)
28. Singh, N., Agarwal, A., Sanghi, S.: Curr. Appl. Phys. **11**, 783–789 (2011)
29. Klinger, M.I.: J. Phys. C, Solid State Phys. **8**, 3595–3607 (1975)
30. Rana, M.U., Islam, M.U., Ishtiaq, A., Abbas, T.: J. Magn. Magn. Mater. **187**, 242 (1998)
31. Yafet, Y., Kittel, C.: Phys. Rev. **87**, 290–294 (1952)
32. Ganguly, A., Mandal, S.K., Chaudhuri, S., Pal, A.K.: J. Appl. Phys. **90**, 5652 (2001)
33. Mohamed, R.M., Rashid, M.M., Haraz, F.A., Sigmund, W.: J. Magn. Magn. Mater. **322**, 2058–2064 (2010)
34. Shaik, M.A., Bellard, S.S., Chougule, B.K.: J. Magn. Magn. Mater. **152**, 391 (1996)
35. Koop's, C.: Phys. Rev. **83**, 121 (1951)
36. Iwachi, K.: Jpn. J. Appl. Phys. **10**, 1520 (1971)
37. Rabinkin, L.I., Novika, Z.I.: Ferrites, p. 145. Minsk (1960)
38. Trivedi, U.N., Chhantbar, M.C., Modi, K.B., Johi, H.H.: Indian J. Pure Appl. Phys. **43**, 688–690 (2005)
39. Singh, A.K., Goel, T.C., Mendiratta, R.G.: J. Appl. Phys. **91**, 6626 (2002)
40. Macdonald, J.R.: Impedance Spectroscopy. Wiley, New York (1987)
41. Ponpandian, N., Balaya, P., Narayanasamy, A.: J. Phys., Condens. Matter **14**, 3221 (2002)